A computational design method for horizontal axis tidal turbines

ABSTRACT

Purpose: A comparative analysis between a straight blade (SB) and a curved caudal-fin tidal turbine blade (CB) is conducted and includes an examination of aspects relating to geometry, turbulence modelling, non-dimensional forces lift and power coefficients.

Design/ methodology/ approach: The comparison utilizes results obtained from a default horizontal axis tidal turbine with turbine models available from the literature. A computational design method was then developed and implemented for 'horizontal axis tidal turbine blade'. Computational fluid dynamics (CFD) results for the blade design are presented in terms of lift coefficient distribution at mid-height blades, power coefficients and blade surface pressure distributions. Moving the CB back towards the SB ensures that the total blade height stays constant for all geometries. A 3D mesh independency study of a 'straight blade horizontal axis tidal turbine blade' modelled using CFD was carried out. The grid convergence study was produced by employing two turbulence models, the standard k-ε model and Shear Stress Transport (SST) in ANSYS CFX. Three parameters were investigated: mesh resolution, turbulence model, and power coefficient in the initial CFD, analysis.

Findings: It was found that the mesh resolution and the turbulence model affect the power coefficient results. The power coefficients obtained from the standard k-ε model are 15% to 20% lower than the accuracy of the SST model. Further analysis was performed on both the designed blades using ANSYS CFX and SST turbulence model. The variation in pressure distributions yields to the varying lift coefficient distribution across blade spans. The lift coefficient reached its peak between 0.75 to 0.8 of the blade span where the total lift accelerates with increasing pressure before drastically dropping down at 0.9 onwards due to the escalating rotational velocity of the blades.

Originality: The work presents a computational design methodological approach that is entirely original. While this numerical method has proven to be accurate and robust for many traditional tidal turbines, it has now been verified further for CB tidal turbines.

INTRODUCTION

Tidal energy is a renewable electricity source that converts the kinetic energy of moving water into mechanical power to drive generators (Shi *et al.,* 2015). This renewable source has minimal CO_2 emissions and is one of the many sources to address concerns over climate change (Tedds *et al.*, 2014). Horizontal axis tidal turbines (HATT) (also known as axial flow turbines) have the rotational axis parallel to the tidal flow and operate in only one flow direction. The mechanical components and principle of HATT operation is similar to the horizontal axis wind turbine (HAWT) – that is, blades are fitted to the hub, a generator converts kinetic energy from the water to mechanical energy, a shaft produces power and a gearbox drives a motor (Bai *et al.*, 2016).

There have been many advances in the development of the computational power and computational fluid dynamics (CFD) models to simulate the complex flow around the turbine (Malki *et al.*, 2014). Several studies conducted in tidal energy have examined the flow effects around turbines (Divett *et al.*, 2013; Funke *et al.*, 2014; Harrison *et al.*, 2010; Blackmore *et al.*, 2016). For example, the characteristics of a 10m diameter three-bladed HATT and the mesh was generated using ANSYS ICEM CFD (12Chord length x 20Chord length of the airfoils used in the rectangular grid); a very fine mesh near the blade wall region was used to obtain precise results but no y+ values (Goundar and Ahmed, 2013). The authors [*ibid*] found that by varying the airfoil's thickness, the blades' hydrodynamic performance and strength improved, with the rotor producing a maximum efficiency of 47.6%. Thrust and power coefficients of a 3D CFD tidal turbine model were validated with

experimental data at 15° and 20° of pitch angle and synergized with the previous work of McSherry *et al.*, (2011). The authors [*ibid*] analyzed the tidal turbine pressure and near-wall effects using shear stress transport (SST) model but also considered the mesh resolution and time step convergence. However, the SST model cannot capture the turbulence 3D effects as the flow passing below the turbine was not modelled by McSherry *et al.*, (2011) (Gayen and Sarkar, 2011; Boris *et al.*, 1992). Subsequently, there are higher 3D turbulence models available which have been rigorously developed and validated against flume tests (Roc *et al.*, 2013; Sescu *et al.*, 2015) but a significant drawback is the computational overhead required to solve the CFD simulation.

A recent study by Divett *et al.*, (2016) presented a methodical numerical simulation of a large tidal turbine array. Hundreds of layouts were simulated using large eddy simulations (LES) to show the linear relationship between total power capture and its increment as additional rows are added onto turbines. The tidal cycle variation is mainly influenced by astronomical factors i.e. the sun and the moon, and the effects of salinity and temperature stratification are secondary factors (Li *et al.*, 2011). Accurately capturing the 3D turbulent flow features of the HATT requires a comprehensive understanding of the physics involved especially when experimental data is missing for validation. Experimental data is expensive to implement and hence, LES provides more flow-physics detail and places less reliance on such data by directly solving the spatially filtered Navier-Stokes equations on the larger turbulent scales (Churchfield *et al.*, 2013; Bin *et al.*, 2013; Ni *et al.*, 2013; Ciri *et al.*, 2016).

This study develops a new computational design methodology for simulating 3D turbulent flow past straight blade (SB) and curved caudal fin blade (CB) HATTs. The design method also conducts a comparative analysis between the prototype blades designed using SST and LES-Smagorisnky turbulence models. The CFD methodology is validated against secondary data available within the literature (Goundar and Ahmed, 2013; Larwood and Zuteck, 2006). By applying this new computational design methodology, the research objective is to augment CFD simulation reliability for the CB tidal turbine blades.

EXISTING CFD MODELLING IN TIDAL ENERGY CONVERSION

Jo *et al.*, (2014) designed a horizontal axis tidal turbine based on the blade element momentum (BEM) method and calculated its efficiency performance to 40%, choosing five as the tip speed ratio. They [*ibid*] also investigated the wake distribution in the unsteady velocity flow affecting the tidal turbine system. CFD analysis was performed using a SST turbulence model and the curves of power coefficient (C_P) and torque generated from the shaft were presented for different velocities. The airfoils were arranged in sequential order with appropriate twist angles and chord lengths to predict the tidal turbine performance using CFD to predict its torque and C_P. Kim *et al.*, (2012) analyzed a bi-directional vertical axis turbine performance in a larger area of tidal channel. Hexahedral mesh was applied in the augmentation channel and an SST turbulence model was selected. The tidal turbine blade performance was accessed based on the pressure and lift coefficients, hence demonstrating the two most significant sensitivities that cause cavitation studies at different angles of attack especially for the leading edge. Rocha *et al.*, (2014) carried out a numerical investigation and calibrated a SST turbulence model to test the operational performance of a small scale horizontal axis wind turbine (SS-HAWT). They [*ibid*] studied aerodynamic performance of the SS-HAWT based on the turbulence intensity and characteristic length (β^*) to reveal the varied effects of friction over the blades.

Afgan *et al.*, (2013) presented a comparison between Reynolds-averaged Navier-Stokes (RANS) models SST and LES numerical solutions for a three bladed HATT, validating the implemented sliding mesh technique for the unstructured mesh code over a range of tip speed ratios (TSRs). The LES solver's accuracy was tested against the optimum design condition to investigate the wake and turbine performance and highlighted issues related to simulations for high rotating velocities. Li *et*

al., (2013) compared three different CFD modelling approaches on a vertical axis wind turbine in higher angles of attack. The NACA 0018 SB foil was simulated using LES with a high angle of attack flow. In symmetrical airfoils the stall angles appear between 10° to 15°. The authors [*ibid*] also commented on the SST turbulence model's efficacy and considered it to be assuring when simulating the adverse pressure gradients in incompressible flow. However, when SST was compared to LES, LES was computationally more challenging but produced more realistic 3D vortex diffusion and flow separation in unsteady flow computations. Force coefficients were calculated in the span wise distribution of the airfoil blades, thus proving LES as a better high fidelity CFD modelling technique. Kang *et al.*, (2012) simulated 3D turbulent flow around an axial tidal turbine, placed on the rectangular bed comprising an open channel accommodating the CFD domain to carry out LES simulations. The convoluted turbine geometry comprising rotor and stator components with moving boundaries were managed by engaging the curvilinear immersed boundary method. The CFD simulations were compared to the marine hydropower turbine using systematic grid refinement and calculating the torque sensitivity analysis. The simulations indicated that pressure fields near the turbine blades generated torque and extracted power from the water column.

The extant literature reveals that the SST model is the most popular turbulence model used in steady state analysis of tidal turbine blades and LES for transient simulations in the absence of experimental data for validation. The literature also illustrates the need for new and alternative/ innovative methodological approaches for the CB design.

A COMPUTATIONAL DESIGN METHODOLOGY
The direct design method represents an optimized approach to product design that requires an understanding of the problem before collecting numerical data for analysis, validation or verification using mathematical modelling (Campi *et al.*, 2002; Shi *et al.*, 2012; Liu, 2010; Wang *et al.*, 2012; Thapar *et al.*, 2011). The direct design method begins by modelling the parametric three-dimensional SB, and then a rectangular mesh domain is generated for inputting the boundary conditions. After defining the boundary conditions, CFD analysis (as a prominent mathematical modelling technique) is performed on the tidal turbine rotors, the numerical results are compared with existing data in the literature. The final step builds the three dimensional model (Figure 1), where chosen turbulence models are tested and verified by further investigation to allow emergence of new data (Hudgins and Lavelle, 1995) The CFD results collected from the SB were comparatively analysed and evaluated with the curved caudal fin shaped blades.

<Insert Figure 1 about here>

The end objectives of the chosen direct blade design method were to: compare the highest power coefficient obtained for the CB with data available within tidal turbine blade literature.

Design of the SB HATT

The SB HATT was designed in ANSYS Design Modeller (refer to Figures 2a; 2b). The airfoil considered for all the horizontal blades is a symmetrical NACA 0018. The spanwise distribution of the airfoils are stationed at every 10% of the blade whilst the distance between hub circle and the root airfoil is 20% of the total blade height.

<Insert Figures 2a and b about here>

The blade hub is circular and its diameter is 40% of the root airfoil chord length. The blade twist angle is higher at the root airfoil because it experiences less rotational forces and it gradually decreases across the entire span of the blade. The SB parameters are given in Table 1.

157
158   <Insert Table 1 about here>
159
160 **Design of the CB**
161 The 3D curved set of centroids defines the shape of the CB. A predictive MATLAB program was
162 created in which the centroids of the NACA airfoil centres form a 3D shape (refer to Figure 3). The
163 MATLAB program computes the centre of mass (gravity) for the set of airfoils used in modelling
164 the CB.
165
166   <Insert Figure 3 about here>
167
168 The weighted centroid uses the pixel intensities in the airfoil region which weights the centroid
169 calculation and the twist angle, which acts as the function of the incremental blade length, is further
170 modified to create a smooth twist by fitting a third order polynomial function. The initial values of
171 the CB NACA profile chord lengths are defined in Table 2 whilst the default profile chosen is
172 NACA 0018.
173
174   <Insert Table 2 about here>
175
176 The X-offset and Y-offset values are used to construct the skeletal (centre line) of the CB. For
177 programming purposes, the nearest third order polynomial regression equation on the centre line
178 curve (refer to Figure 4) is defined as:
179
180   <Insert Figure 4 about here>
181
182 Each NACA profile centre is built on the centre line which acts as a master and each profile datum
183 sits along its length divided by the height - the numbers of stations stay constant to reduce the
184 computational overhead. The NACA profile sections of the curved blade are considered parallel to
185 the x-axis, that is, the normal of each NACA section should be the y-axis. The skeleton which is
186 fitted on the midpoint of the each airfoil has a decrease in the chord length in the blade spanwise
187 direction which increases the surface area of the CB. The third order polynomial is fitted on the
188 skeleton of the caudal fin centerline, starting at the airfoil root centre and passing through all the
189 airfoil stations to the tip of the airfoil; at this end of the blade, bending occurs to create the CB. The
190 chord lengths of the SB can be varied in linear or non-linear progression along the span-wise
191 direction to reach the CB (refer to Figure 5).
192
193   <Insert Figure 5 about here>
194
195 ***Strategy to Move the Curved Blade Shape Backwards to SB Shape***
196 The polynomial centre-line from the root chord was moved in the percentage chord lengths in order
197 to reach the target shape. For the initial experimentation, the percentage chord lengths were moved
198 in 0%, 25%, 50%, 75%, and 100% increments; where 0% represents the initial SB chord lengths.
199 For convenience during experimentation, the same blade is simulated whilst the total blade height
200 and number of stations are kept constant until the best design is found (i.e. maximum power
201 coefficient of the blade system). The tidal turbine blade power coefficient is predominantly
202 sensitive to total blade height but also blade twist and chord length distribution - changing the value
203 of each and every design variable would be time consuming. To overcome this problem, repetitive
204 transformations of the default blade design method was used. Using this approach, the percentage
205 based chord lengths were selected and the third order polynomial function remains constant
206 ensuring that the blade span or total blade height will replicate the default SB. Thus it was possible
207 to define a design study strategy that moved the target shaped CB backwards to the SB shape using
208 a linear progression function which can be demonstrated as follows:

4

$$T_{ASTN} = T_{SXC} \times \left(\frac{R_P}{100}\right)$$

Equation 1

Where: T_{ASTN} is the required airfoil station value; T_{SXC} is the target shape X-coordinate value for the particular airfoil station; and R_p is the required chord length percentage. After calculating the X and Y-offsets for the blade spinal axis variation, the backward design strategy can be plotted in Figure 6.

<Insert Figure 6 about here>

A COMPARATIVE ANALYSIS BETWEEN THE FIVE DESIGNED PROTOTYPE BLADES

Figure 7 illustrates the rectangular computational grid which was used to model the seawater domain and the turbine disc domain, for the SB and CB geometries. The seawater domain extends five times the turbine diameter at the inlet, ten times of the turbine diameter at the outlet whilst the height of the rectangular grid is five times of the turbine diameter. The turbine domain was designed as a rotating domain in CFX and then a full 360° mesh surrounding the tidal turbine blades. Figure 7 shows blade automated meshing including the hub and tips of the SB and the CB.

<Insert Figure 7 about here>

Mesh Independency study

To establish the accuracy of the CFD solution, and to keep the computational costs low, the straight blade was analysed using: the standard k-ε model, and SST model, at uniform V_{in} = 2.5m/s, and λ = 5. The grid convergence study was performed by developing three different meshes: with a coarse, medium, and fine grid for all six different meshes of the Straight Blade to predict the power, lift coefficients, and torque on normalised mesh cells to determine how the mesh quality affects CFD simulation results.

The number of nodes and the simulation time for the three cases simulated using the SST model are highlighted in Table 3, and the three cases simulated using the standard k-ε model are given in Table 4. Table 3, and 4 summarise the key characteristics of the meshes, and it is very clear that CFD simulation time is highly dependent on the number of mesh nodes considered. The six meshes generated have near wall resolution i.e. y+ < 10 by using the standard wall function approach to avoid unsatisfactory results when using the standard k – ε model.

<Insert Table 3 about here>

<Insert Table 4 about here>

In the case of the investigated meshes of the straight blade, the turbine domain has an increased mesh resolution. The mesh is refined in the grids from M1 to M6 where M1, M2, M3 represent coarse, medium, and fine mesh generated for the SST turbulence model; and M4, M5, M6 represent coarse, medium, and fine mesh generated for the standard k-ε turbulence model. The estimated power coefficient increased from 0.2271 to 0.4218 as shown in Figure 8.

<Insert Figure 8 about here>

It is important to note that the mesh resolution plays a pivotal role in the final CFD results. The mesh nodes need to be small to resolve the boundary layer on the blade surfaces. The highest CP obtained from the mesh independent study is 0.4218 for M3 from the SST model. M2 and M3

account for nearly 1% difference in the estimated power coefficients, but the final CFD simulation time required for convergence of the two meshes has a significant difference when the conventional mesh independency method is employed. The power coefficients obtained from the standard k-ε model are almost 15% to 20% lower than the SST model power coefficients, which is due to the poor performance of the k-ε model in near-wall regions and in adverse pressure gradients i.e. the fluid flow near the turbine blade surfaces; which causes the k-ε model to underestimate the power coefficient.

It is clear from the final CFD simulation results that the simulation time is highly dependent on the number of mesh nodes, and the turbulence model selected. As shown in Figure 8 when using k-ε model for all the meshes (M4, M5, and M6) employed the CFD solution under predicts power coefficient when compared with the SST model. M1 leads to the reasonable prediction of the power coefficient on the straight blade, whereas the power coefficient of M3 is slightly better than M2. Due to the slight difference, medium mesh (M2) is best regarding computational costs and is further employed for the numerical analysis carried out in the following section of the turbulence model comparison study.

Turbulence model comparison study
To understand the sensitivity of the CFD solution a consecutive study was carried out with these turbulence models at medium sized meshes. From the mesh dependency test conducted it has been found that the SST model performs superiorly in adverse pressure gradient situations than the standard k-ε model; because SST model is a unification of k-ε model and k-ω model for free stream and inner boundary layer problems respectively. Figure 9 shows the torque coefficient related to each of the two turbulence models analysed for the medium mesh. As shown in Figure 9 the SST model medium mesh has higher CM than the standard k-ε model in all the nine different TSR's. It can also be seen that the torque coefficient of SST medium mesh model increased by more than 25% when compared to the standard k-ε model medium mesh.

<Insert Figure 9 about here>

The highest CM is achieved at λ= 5 for both the cases, CM increases with the increasing TSR and acts as a function of TSR. It can also be noted that the non-linearity in the torque coefficient occurs after TSR of 5, and the k-ε model fails to capture this, due to the boundary layer and turbulence quantities to the blade wall.

Figure 10 shows that the power coefficient increases steadily until TSR ≈ 5, at which it shows the peak CP ≈ 0.4169 for the SST model medium mesh; after which it shows a drastic reduction with the increasing λ > 6. The curve for medium mesh the k-ε model shows that it predicts a lower power coefficient to a satisfying level of accuracy, and also under predicts the values with increasing λ. However, the numerical CP prediction by medium mesh the SST model observed values are approximately 20% higher than medium mesh the k-ε model simulation, the range $5 \leq \lambda \leq 6$ was also validated (Bahaj et al., 2007; McSherry et al., 2011); and considered to be optimum range for HATT. The standard k-ε model is incapable of capturing the account of rotational forces and their effects on the turbine blades, and due to the near wall physics implementation. Thus the CP prediction by SST model is more acceptable when compared to the power coefficient predictions by the standard k-ε model.

<Insert Figure 10 about here>

As a result of the mesh independency test conducted it can be concluded that the overall power coefficient shown by the SST turbulence model is more reasonable than the standard k-ε model, for all the cases considered. Therefore to avoid any misleading CFD results the standard k-ε model is

309 not employed in any further CFD tests conducted in this research. The power coefficient of a HATT
310 is highly sensitive to the turbulence model chosen for the CFD analysis; however the mesh
311 independent CFD solution for SST medium mesh satisfactorily achieves the mesh independency
312 over the SST fine mesh solution which requires a massive computational overhead. Hence, the
313 medium mesh is used to conduct the steady state analysis in following sections.
314
315 **Steady state CFD analysis**
316 The steady state simulations were conducted using ANSYS CFX via the SST turbulence model. In
317 ANSYS CFX, the pressure-velocity coupling was achieved using the Rhie - Chow Option, and all
318 the interpolation and advection values were set at high resolution. In the meshing aspect, some
319 controls were modified to suit the concentration on the curved shaped blades because of the
320 additional bend on the surface. Table 5 summaries the blade model functions and the respective
321 characteristics.
322
323   <Insert Table 5 about here>
324
325 Table 3 illustrates that the number of nodes of the CB 100% case study are almost twice that of the
326 SB case study – this is due to the flow being considerably complicated and the blade surfaces being
327 bent for the curved blade shape. The three-dimensional modelling and steady state CFD simulations
328 presented are conducted at constant inlet velocity of 2.5m/s, using high turbulence intensity of 10%.
329 The outlet pressure was defined as 0bar, the blade was defined as a *rotating wall*, with no slip wall
330 condition for mass and momentum option. The bottom and side walls were defined as free slip
331 walls to incorporate accuracy when solving the continuity equation. The front and back walls were
332 defined as inlet and outlet walls respectively. As the seawater flow velocity progressed over the
333 blade pressure side, the pressure increased especially on the tip of the blade where rotational
334 velocity was at its highest point. Figure 11 shows the comparison of the blade pressure distribution
335 on the case studies performed (blades rotate anti-clockwise).
336
337   <Insert Figure 11 about here>
338
339 Data accompanying Figure 11 compares the steady-state pressure distribution on the five blade
340 designs. Numerical simulations show how the seawater flow behaves on the trailing and leading
341 edges on the pressure side of the blade. The varying lift coefficient distribution is also demonstrated
342 by plotting the blade mid-span coefficient of lift distributions for all five blade designs. CB 75%
343 shows the highest lift coefficient at 0.5 blade span location with a peak value of 0.182 while CB
344 100% shows the lowest lift coefficient value of 0.0835 amongst all the blades designed.
345 Interestingly, Figures 11 and 12 illustrate that the pressure is higher on the outer radius of trailing
346 edge of the CB 100% (target shape blade), as compared to the other four blade geometries. This
347 may be because the target shape is modelled as an assumption of the fish caudal fin and generates
348 flow reattachment. Pressure near the tip region of all five designs increases as compared to the rest
349 of the blade and the leading edge contributes to the pressure distribution increase on the pressure
350 side. Simultaneously, the trailing edge causes negative pressure distribution increase on the suction
351 side which contributes to lift force decrement and torque force reduction.
352
353   <Insert Figure 12 about here>
354
355 Figure 12 illustrates that variations in the pressure distribution yield the varying lift coefficient
356 distribution on the airfoil chord length. The lift coefficient increases with the increase in blade span
357 until 0.8 blade span location, after which a drastic reduction near the blade tip occurs. Although the
358 lift coefficient varies in magnitude for all the blade designs, it can be observed that the CB 100%
359 results in lower lift coefficients when compared to the other four blade designs. Therefore, it can be
360 concluded from the steady state analysis that the target shape blade (i.e. CB 100%) would cause

7

drag increase. This would cause torque reduction, leading to a lower power coefficient as the bend on the blade increases.

Transient CFD analysis

Transient simulations for the five blade designs were generated using the LES-Smagorinsky sub-grid scale model and fine unstructured mesh in an integrated time step. For all five design LES cases, the time step used for the simulation required for the flow to pass entirely through the turbine was about 0.15million time steps. The time step size for each case was set to 3 x 10^{-5} which coincides with approximately ten blade rotations for the TSR = five for all five cases, which is equivalent to 4.89 x 10^5 seconds or 135.83 hours. Multiple frames of reference (MFR) was applied to the turbine disc analysis as it was a rotating domain based on the general grid interface (GGI) available in CFX. The turbulence intensity at the inlet of the computational domain was defined as 15% (typical seawater value) and as the tidal turbine blade geometry is a high turbulence intensity case. It should be noted that the non-uniform velocity of 2.5 m/s was applied to all five blade designs. The turbulence intensity gradually decreased at a distance of four rotor diameters downstream from the inlet to 13.68% due to velocity instability, and the turbulence level at the rotor leading edge was observed to be 12.82%. This gradual decrease was expected due to the higher rotational velocity of the blades which correspond to the blade tip. At the solid boundaries (blade geometry) the near wall node was $y^+ = 50 < y+ < 300$ (Piomelli and Balaras, 2002; Tessicini and Leschziner, 2007) because of the two zonal layer LES approach used and the refined fine mesh in the tidal turbine domain was embedded into the ocean flow domain. The mesh parameter values for LES- Smagorinsky simulations are reproduced in Table 6.

<Insert Table 6 about here>

The residuals convergence criterion for each time step was set to 10^{-5} and two monitors were used namely (Oberkampf *et al*., 2004; Lim *et al*., 2012; Versteeg and Malalasekera, 2007):

- Scaled residual monitors for mass and momentum of the iterative process; and
- Lift coefficient C_L trend as a function of the iteration number for LES-Smagorinsky solution.

The CFD solution is considered to have converged when the mass and momentum residuals present a constant trend under 10^{-5} value which is illustrated in Figure 13 where the residuals represent the downward trend of the scaled residuals for the CB 75% LES-Smagorinsky solution.

<Insert Figure 13 about here>

Figure 13 illustrates that the residuals mark the continual removal of the unwanted imbalances thereby causing the CFD iterative process to converge rather than diverge. The mass residual at the time step number 1795 reached the convergence value of 7.269e^{-06} and 9.51e^{-06} on the time step 2665 when the transient solution was stopped. The discretised mass and momentum equations are presumed to be converged when they reached the convergence criterion and did not change with further iterations. The mass flow balance between the inlet and outlet were also verified for all the transient CFD simulations performed to ensure continuity of the solution (CFX-Solver Theory Guide, 2009; Oberkampf and Trucano, 2000). The lift coefficient (C_L) history over iterations was also monitored to check the unsteady convergence of the LES-Smagorinsky solution (refer to Figure 14 for CB 75%). There was no appreciable change observed in the lift coefficient after 1100 timesteps but the solution was still monitored for more than 1500 time steps as the lift coefficient elevations to the fixed value of 0.1795.

<Insert Figure 14 about here>

LES transient simulations conducted sought to compare the results obtained with the steady state SST simulations. The turbine pressure contours (LES-Smagorinsky) (Figure 15) illustrate that a difference between the pressure and suction sides of the blade becomes smaller as the rotational velocity increases on the upper part of the blade. In comparison to steady state simulations, this increases the net lift and torque.

<Insert Figure 15 about here>

The pressure prediction on the tip of the blade (where the rotational velocity of the blade is at its highest) also causes higher lift on the pressure side of the blade. Figure 16 reveals that lift distribution on the suction side of the mid-height is larger than on the pressure side of the airfoil. This scenario significantly increases drag force on the CB 100% (target shape) as compared to the other four geometries, making it directly proportional to the bend on the blade. It also illustrates that the most affected region by the seawater is the tip chord of the blade along leading and trailing edges. The drag increment for the CB 100% was expected seeing the negative pressure on the suction side on the tip, proving to generate cavitation in extreme velocity conditions.

<Insert Figure 16 about here>

The LES simulations demonstrate that the kinetic energy contained in the seawater flow is extracted from the blade's upper stream and that pressure prediction is more realistic as there is no flow divergence in real life HATT's. The prediction of the lift caused due to the large separation of the flow and the pressure surface of the blades consequently increases the predicted power coefficients, and causes less discrepancy in the vorticity of the pressure field. Interestingly, LES solutions with a high computational overhead demonstrate a clear phenomenon of the pressure changes on the blade and avoids over prediction of the lift and power coefficient.

DISCUSSION OF THE COMPARISON BETWEEN THE DESIGNED BLADES
The performance of SST and LES-Smagorinsky turbulence models are examined by plotting the lift coefficient against various angles of attack (refer to Figure 17). There is a gradual decrease in the lift coefficient after the six degrees of angle of attack for all the cases, as the flow becomes highly non-linear and the rotational velocity of the blades reaches its maximum. The mass flow rate of the seawater is a function of the cross-sectional area of the turbine blades and its velocity, therefore the bend on the curved blades makes the mass flow rate drop the lift coefficient after 6 degrees of angle of attack.

<Insert Figure 17 about here>

Therefore, it can be concluded that with the increase in the angle of attack the turbine blades would rotate faster but simultaneously kinetic energy available in the seawater exerts a drag force upon the blade, causing a reduction of the overall power coefficient of the turbine blade. The output power notably depends on the inlet seawater velocity (refer to Figure 18). Although the CB 100% yields almost 15% more power than the SB in case of all the flow velocities, this does not necessarily mean that it would yield the highest power coefficient for the designed blades.

<Insert Figure 18 about here>

The SB produces 366 kW of power and a power coefficient of 0.4028, whilst the CB 100% provides approximately 20% more output power than the SB, and about 15% more power than the most efficient CB 75%. However, the power coefficient for the target shape blade i.e. CB 100% is 0.3951 and 0.3728 for the SST and LES-Smagorinsky CFD simulations respectively. As 80% of turbine blade efficiency (i.e. the power coefficient) is generated from the midsection of the designed blade to the tip of the blade. The CB 75% showed the most consistent and efficient set of data from

9

the SST and the LES-Smagorinsky CFD tests. There was little difference between the results from the LES-Smagorinsky CFD simulations but these results confirm the accuracy of the comparative analysis while using two different turbulence modelling techniques. Therefore, the CB 75% will be put forward to allow the coefficient power comparison with the standard (suitable) HATT models available in the tidal turbine literature.

Goundar and Ahmed (2013) designed a three bladed 10m diameter HATT, and achieved a maximum efficiency of 47.5% with a power output of 150kW, for the constant seawater velocity of 2m/s. The CB 75% is also three bladed and has a 14.2 diameter, and yields an efficiency of 51.78% for LES simulations with a power output of 435kW; which is higher than the overall efficiency achieved by Goundar and Ahmed [9]. At the same time the benefit of designing a blade like a CB generates higher lift and power coefficients at lower and higher tidal current velocities, and this has been demonstrated with the CFD simulations presented above. The STAR blade to generate low-cost electricity from wind designed by Larwood & Zuteck (2006) implements swept blade design parameters and produces annual power output which ranges from 1.5 to 3MW. The designed turbine blades are 71 to 126m in diameter and have rated generator speed of 1800rpm, and the designed swept wind turbines produce 10 to 15% more power than the standard wind turbines available in the current market. A direct comparison between the results obtained from this research with the STAR blade is beyond the scope of this research, as the maximum diameter a tidal turbine can have 22m (Bahaj *et al*., 2007; Bahaj *et al*., 2007; Batten *et al*., 2008), and as the designed CB 75% is 14.4m in diameter. A general comparison of the annual power output can be made, i.e. designing the curved caudal fin blades produces at least 10% more annual power output than the standard straight blades which has been shown by both the studies i.e. by this research and by Larwood & Zuteck (2006).

In summary, analysis results confirms that bio-mimicking the caudal fin look-alike turbine blade i.e. CB 75%, produces greater efficiency than the default SB which was designed according to the tidal turbine blade literature and meets the aim of this paper.

CONCLUSIONS

It can be concluded that although LES-Smagorinsky provides a better result than the SST simulations, it also has a massive computational overhead. The CFD results allow a further comparison of the power coefficients; proving that a CB produces more efficiency than the standard HATT's at lower and higher tidal current velocities. The most fundamental challenge confronting this research was to validate the CFD methodology for the case studies performed with real world data. This is also the most significant problem faced in the wind turbine industry, to which this research could contribute. To overcome this challenge, a comparative analysis was performed for the SB and CB 75% with the tidal turbine literature which thus helps the future tidal turbine blade designers in knowledge transfer, particularly on turbulence model selection. A mesh independency study of a straight blade to determine the mesh sensitivity and its effects on the CFD simulation results. The grid convergence study was simulated using two turbulence models: the standard k-ε model, and SST turbulence model at coarse, medium, and fine mesh resolution thus simulating six different mesh sizes. This paper has shown that obtaining mesh independent solutions is a fundamental need for all the tidal turbine blade designers due to the sensitivity of the lift coefficient of the tidal turbine.

The standard k-ε model under predicts the power coefficients and the simulation time is highly dependent on the mesh and turbulence model chose for CFD analysis. The highest CP obtained from the mesh independent study conducted is 0.4218 for M3 from SST model and the lowest CP 0.2693 for M6 using k-ε model. M2 and M3 account for nearly 1% difference in the estimated power coefficients, but the final CFD simulation time required for convergence of the two meshes is substantially different when conventional mesh independency method is employed. Pressure distribution is a predominant output for determining the lift, and power coefficients, and also to define the most efficient blade. Lift coefficient distribution across blade spans showed a similar

516 trend of the peak lift coefficient being observed at 0.75 to 0.8 of the total blade span before
517 drastically dropping down at 0.9 onwards due to the increasing rotational velocity of the blades.
518
519 The unsteady convergence is an iterative process of the transient solution which needs to be
520 monitored to calculate the accuracy of the transient CFD solution. This was done by monitoring the
521 scaled residuals for mass, and momentum and observing lift coefficient as a function of the
522 iteration. The removal of unwanted imbalances over time steps result in the CFD solution to
523 converge and do not change with further iterations. Future work derived from the observations
524 made from this research should seek to develop a design automation closed loop system using
525 Knowledge Based Engineering (KBE) principles to design a robust tidal turbine blade design which
526 would be optimal throughout the year. The designed closed loop system would automatically
527 parameterize blade geometry, generate automatic mesh, and the numerical results by itself.
528

529 **REFERENCES**
530 Afgan I, McNaughton J, Rolfo S, Apsley DD, Stallard T, Stansby P. (2013) Turbulent flow and
531   loading on a tidal stream turbine by LES and RANS. *International Journal of Heat and Fluid*
532   *Flow*. Vol. 43, pp. 96–108.
533 ANSYS INC. CFX-Solver Theory Guide 2009.
534 Bahaj AS, Batten WMJ, McCann G. (2007) Experimental verifications of numerical predictions for
535   the hydrodynamic performance of horizontal axis marine current turbines. *Renewable Energy*.
536   Vol. 32, pp. 2479–90.
537 Bahaj AS, Molland AF, Chaplin JR, Batten WMJ. (2007) Power and thrust measurements of marine
538   current turbines under various hydrodynamic flow conditions in a cavitation tunnel and a towing
539   tank. *Renewable Energy*. Vol.32, pp. 407–26.
540 Bai G, Li W, Chang H, Li G. (2016) The effect of tidal current directions on the optimal design and
541   hydrodynamic performance of a three-turbine system. *Renewable Energy*. Vol. 94, pp. 48–54.
542 Batten WMJ, Bahaj AS, Molland AF, Chaplin JR. (2008)The prediction of the hydrodynamic
543   performance of marine current turbines. *Renewable Energy*. Vol. 33, pp. 1085–96.
544 Bin JI, LUO X, PENG X, WU Y. (2013) Three-dimensional large eddy simulation and vorticity
545   analysis of unsteady cavitating flow around a twisted hydrofoil. *Journal of Hydrodynamics*.
546   Vol.25, pp. 510–9.
547 Blackmore T, Myers LE, Bahaj AS. (2016) Effects of turbulence on tidal turbines: Implications to
548   performance, blade loads, and condition monitoring. *International Journal of Marine Energy*.
549   Vol. 14, pp. 1–26.
550 Boris JP, Grinstein FF, Oran ES, Kolbe RL. (1992) New insights into large eddy simulation. Fluid
551   Dynamics Research. Vol. 10, pp. 199–228.
552 Campi MC, Lecchini A, Savaresi SM. (2002) Virtual reference feedback tuning: a direct method
553   for the design of feedback controllers. *Automatica*. Vol.38, pp. 1337–46.
554 Churchfield MJ, Li Y, Moriarty PJ. (2013) A large-eddy simulation study of wake propagation and
555   power production in an array of tidal-current turbines. *Philos Trans R Soc London A Math Phys*
556   *Eng Sci*. Vol. 371:20120421
557 Ciri U, Rotea M, Santoni C, Leonardi S. (2016) Large Eddy Simulation for an array of turbines with
558   Extremum Seeking Control. American Control Conference, Boston, MA, USA, pp. 531–6.
559 Divett T, Vennell R, Stevens C. (2013) Optimization of multiple turbine arrays in a channel with
560   tidally reversing flow by numerical modelling with adaptive mesh. *Phil Trans R Soc A*. Vol.
561   371, 20120251.
562 Divett T, Vennell R, Stevens C. (2016) Channel-scale optimisation and tuning of large tidal turbine
563   arrays using LES with adaptive mesh. *Renewable Energy*. Vol. 86, pp. 1394–405
564 Funke SW, Farrell PE, Piggott MD. (2014) Tidal turbine array optimisation using the adjoint
565   approach. *Renewable Energy*. Vol. 63, pp. 658–73.
566 Gayen B, Sarkar S. (2011) Direct and large-eddy simulations of internal tide generation at a near-
567   critical slope. *Journal of Fluid Mechanics*. Vol. 681 pp. 48–79.
568 Goundar JN, Ahmed MR. (2013) Design of a horizontal axis tidal current turbine. *Applied Energy*.
569   Vol. 111, pp. 161–74.
570 Harrison ME, Batten WMJ, Myers LE, Bahaj AS. (2010) Comparison between CFD simulations
571   and experiments for predicting the far wake of horizontal axis tidal turbines. *IET Renewable*
572   *Power Genereration*. Vol. 4, pp. 613–27.
573 Hudgins DW, Lavelle JP. (1995) Risk management in design engineering bids. University of North
574   Texas Libraries, Digital Library, Kansas City, Missouri.
575 Jo C-H, Lee J-H, Rho Y-H, Lee K-H. (2014) Performance analysis of a HAT tidal current turbine
576   and wake flow characteristics. *Renewable Energy*. Vol. 65, pp. 175–82
577 Kang S, Borazjani I, Colby JA, Sotiropoulos F. (2012) Numerical simulation of 3D flow past a real-
578   life marine hydrokinetic turbine. *Advances in Water Resources*. Vol. 39, pp. 33–43.
579 Kim K-P, Ahmed MR, Lee Y-H. (2012) Efficiency improvement of a tidal current turbine utilizing
580   a larger area of channel. *Renewable Energy*. Vol. 48, pp. 557–64.

581   Larwood S, Zuteck M. (2006) Swept wind turbine blade aeroelastic modeling for loads and
582   dynamic behavior. *AWEA Wind.* pp. 1–17.
583   Li C, Zhu S, Xu Y, Xiao Y. (2013) 2.5 D large eddy simulation of vertical axis wind turbine in
584   consideration of high angle of attack flow. *Renewable Energy*. Vol. 51, pp. 317–30.
585   Li M, Radhakrishnan S, Piomelli U, Rockwell Geyer W. (2010) Large-eddy simulation of the tidal-
586   cycle variations of an estuarine boundary layer. *Journal of Geophysical Research Ocean*. Vol.
587   115.
588   Liu P. (2010) A computational hydrodynamics method for horizontal axis turbine--Panel method
589   modeling migration from propulsion to turbine energy. *Energy*. Vol. 35, pp. 2843–51.
590   Malki R, Masters I, Williams AJ, Croft TN. (2014) Planning tidal stream turbine array layouts using
591   a coupled blade element momentum--computational fluid dynamics model. *Renewable Energy*.
592   Vol. 63, pp. 46–54.
593   McSherry R, Grimwade J, Jones I, Mathias S, Wells A, Mateus A. (2011) 3D CFD modelling of
594   tidal turbine performance with validation against laboratory experiments. 9th European Wave
595   Tidal Energy Conference, University of Southampton, UK.
596   Mo J-O, Choudhry A, Arjomandi M, Lee Y-H. Large eddy simulation of the wind turbine wake
597   characteristics in the numerical wind tunnel model. *Journal of Wind Engineering and Industrial
598   Aerodynamics*. Vol. 112, pp. 11–24.
599   Oberkampf WL, Trucano TG, Hirsch C. (2004) Verification, validation, and predictive capability in
600   computational engineering and physics. *Applied Mechanics Reviews*. Vol. 57, pp. 345–84.
601   Oberkampf WL, Trucano TG. (2000) Validation methodology in computational fluid dynamics.
602   Fluids 2000 Conference and Exhibit Denver,CO,U.S.A. pp. 19–22.
603   Piomelli U, Balaras E. (2002) Wall-layer models for large-eddy simulations. *Annual Reviews in
604   Fluid Mechanics*. Vol. 34, pp. 349–74.
605   Roc T, Conley DC, Greaves D. (2013) Methodology for tidal turbine representation in ocean
606   circulation model. *Renewable Energy*. Vol. 51, pp. 448–64.
607   Rocha PAC, Rocha HHB, Carneiro FOM, da Silva MEV, Bueno AV. (2014) k-ω SST (shear stress
608   transport) turbulence model calibration: A case study on a small scale horizontal axis wind
609   turbine. *Energy*. Vol. 65. pp. 412–8.
610   Sescu A, Meneveau C. (2015) Large-Eddy Simulation and Single-Column Modeling of Thermally
611   Stratified Wind Turbine Arrays for Fully Developed, Stationary Atmospheric Conditions.
612   *Journal of Atmospheric and Oceanic Technology*. Vol. 32, pp. 1144–62.
613   Shen H, Li S, Chen G. (2012) Quantitative analysis of surface deflections in the automobile exterior
614   panel based on a curvature-deviation method. Journal of Materials Processing Technology. Vol.
615   212, pp. 1548–56.
616   Shi W, Wang D, Atlar M, Guo B, Seo K. (2015) Optimal design of a thin-wall diffuser for
617   performance improvement of a tidal energy system for an AUV. *Ocean Engineering*. Vol. 108,
618   pp. 1–9.
619   Tedds SC, Owen I, Poole RJ. (2014) Near-wake characteristics of a model horizontal axis tidal
620   stream turbine. *Renewable Energy*. Vol. 63, pp. 222–35.
621   Tessicini F, Li N, Leschziner MA. (2007) Large-eddy simulation of three-dimensional flow around
622   a hill-shaped obstruction with a zonal near-wall approximation. *International Journal of Heat
623   and Fluid Flow*. Vol.28, pp. 894–908.
624   Thapar V, Agnihotri G, Sethi VK. (2011) Critical analysis of methods for mathematical modelling
625   of wind turbines. *Renewable Energy*. Vol. 36, pp. 3166–77.
626   Versteeg HK, Malalasekera W. (2007) *An introduction to computational fluid dynamics: the finite
627   volume method*. 2nd edition, Pearson Education, Essex, England.
628   Wang J, Piechna J, Mueller N. (2012) A novel design of composite water turbine using CFD.
629   Journal of Hydrodynamics. Vol. 24, pp. 11–6.

630

631

632

633

634

635

636

637

638

639

640 **Figure 1** - Graphical Overview of the Direct Design Method Used
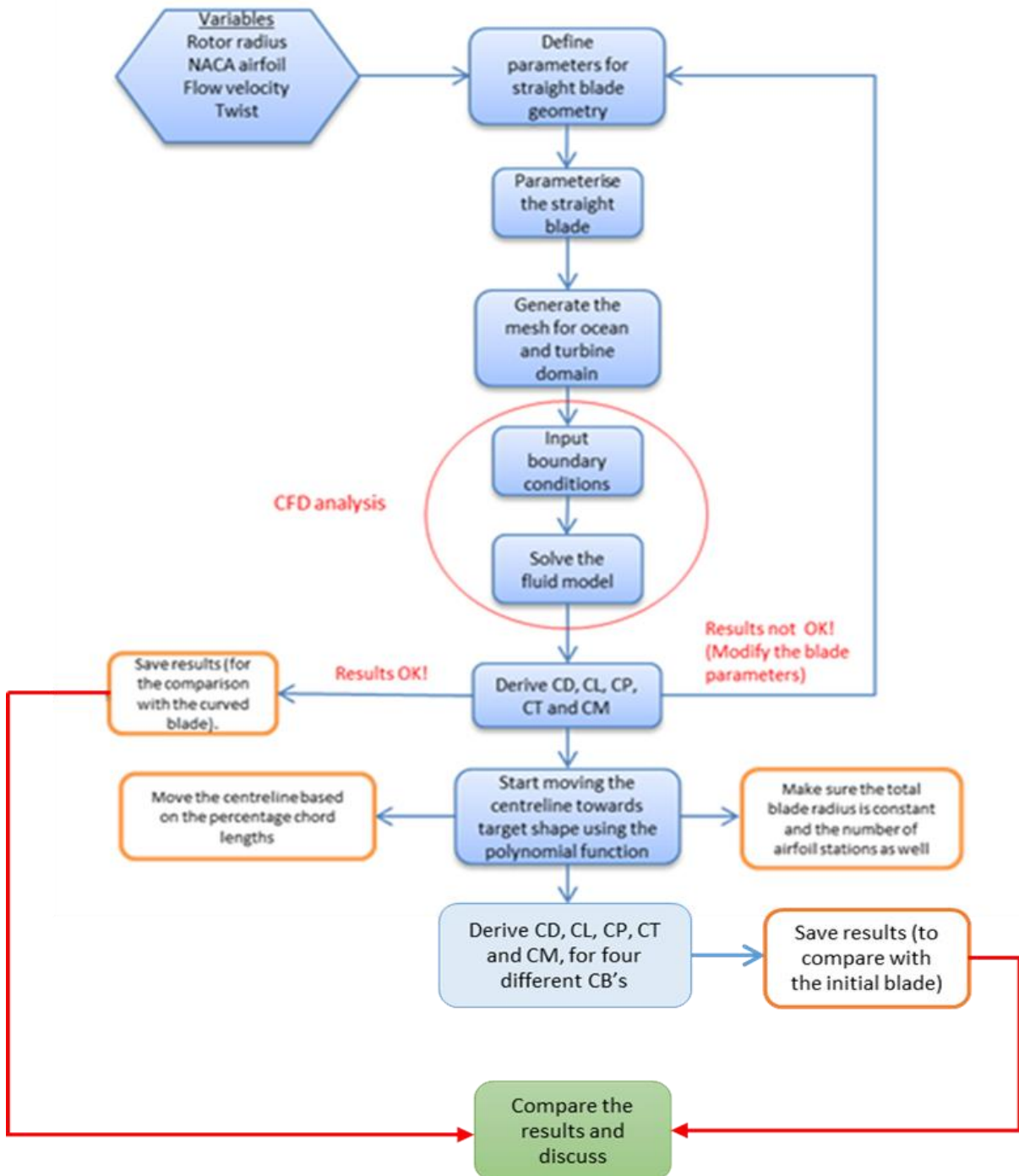
641

642
643

644   **Figure 1(a)** - 3D Model of the SB HATT; **2(b)** Non-linear Twist Distribution
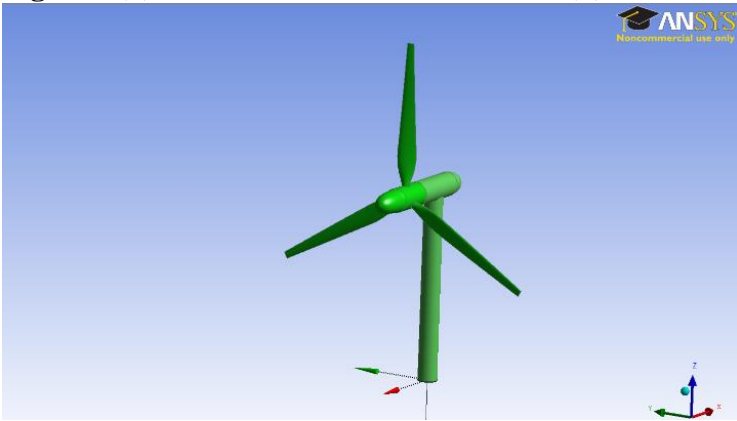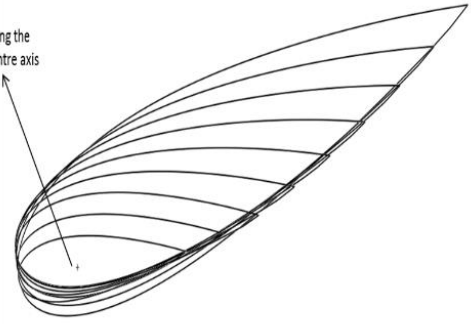
645
646

647 **Table 1** - SB Parameters

Number of blades	3
Radius	7.4 m
Airfoil	NACA 0018
Root airfoil chord length	1 m
Tip airfoil chord length	360 mm
Root airfoil twist	16°
Tip airfoil twist	4°

648
649

650   **Figure 3** - 3D Plot of the CB Reproduced by MATLAB Program
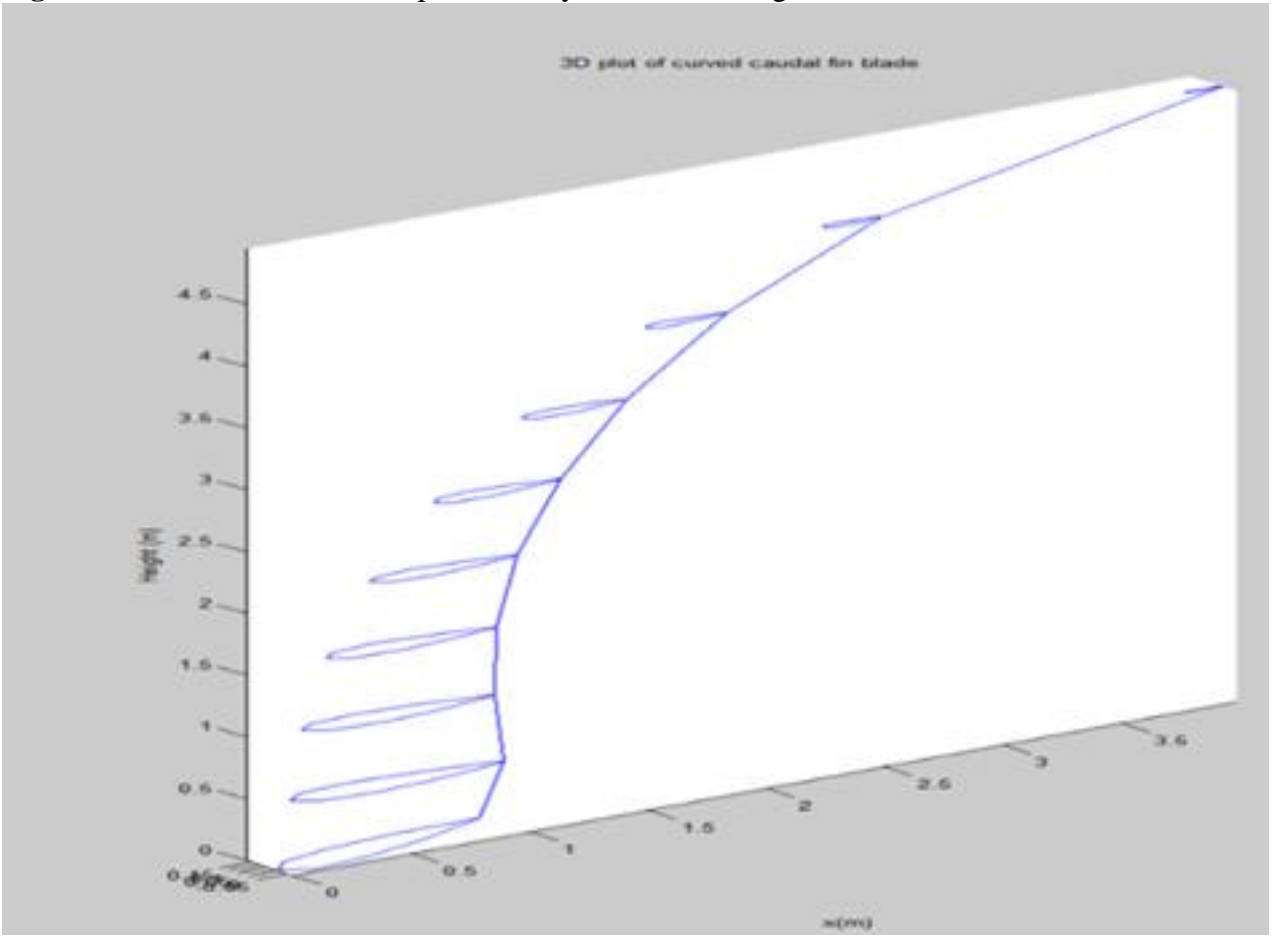
651
652

653 **Table 2** - Default Values for Defining the Curved Blade Shape
654

X- Offset	Y – Offset	Chord length, c (mm)
0	0	1645
0.2285	0.6	1337
0.4998	1.2	1091
0.8145	1.8	924
1.197	2.4	808
1.678	3	663
2.2164	3.6	509
2.7833	4.2	353
3.489	4.8	0

655
656
657

658   **Figure 4** - The Skeleton (Centre Line) of the CB Fitted with Third Order Polynomial Function

$$x = 0.0034y^3 + 0.0678y^2 + 0.3209y + 0.0043$$
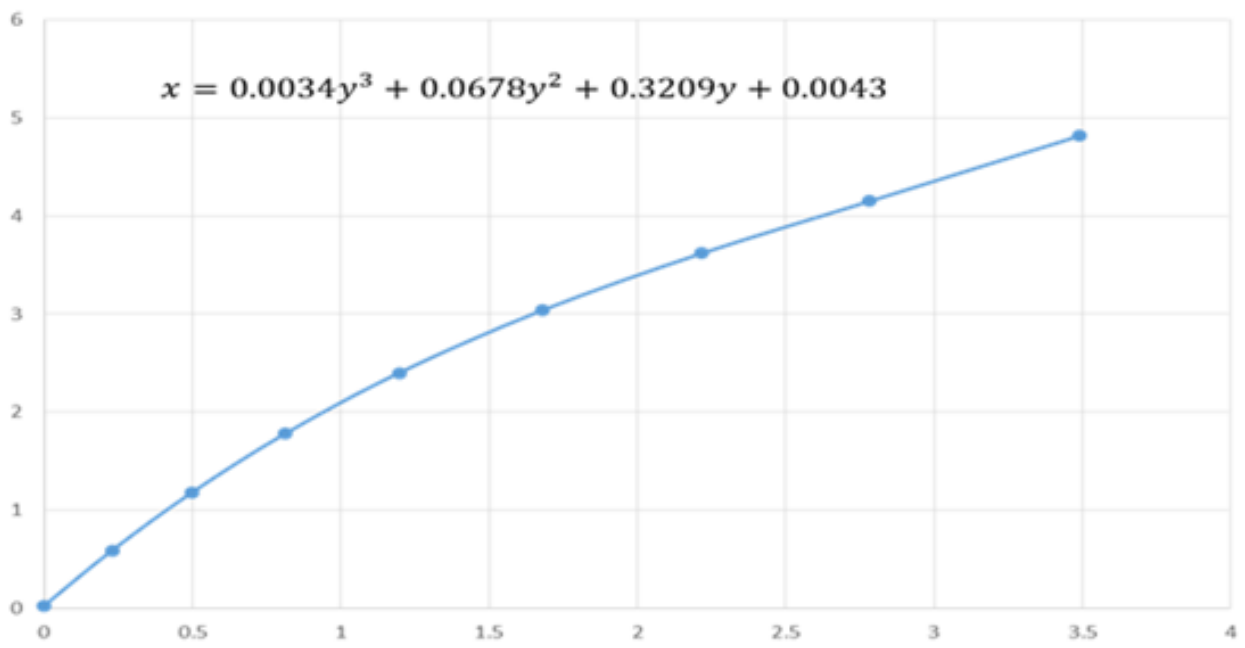
659
660
661
662
663

664 **Figure 5** - Chord Length Variation of the SB to Achieve CB
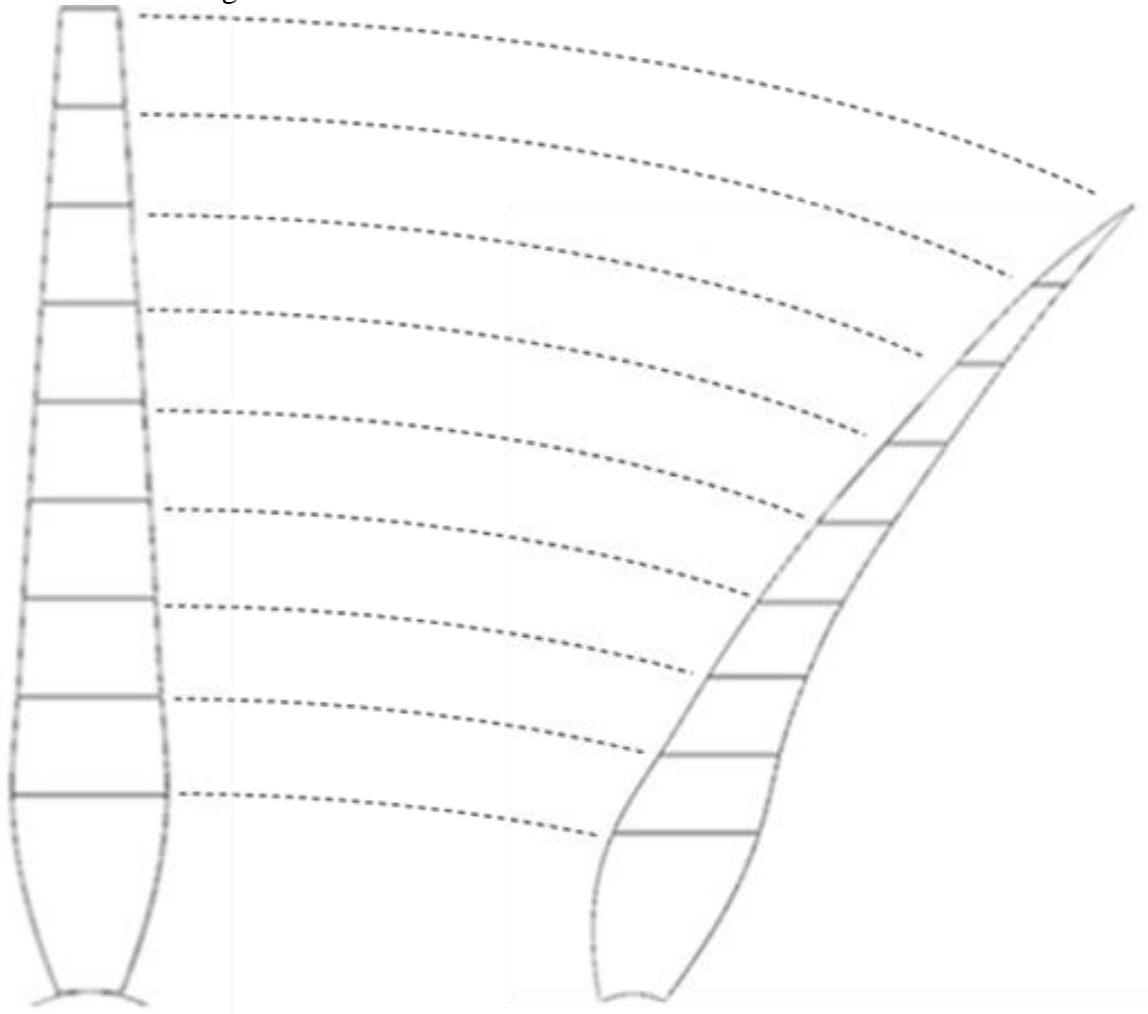
665
666
667

668   **Figure 6** - Blade Spinal Axis Variation

Figure 6 - Blade Spinal Axis Variation
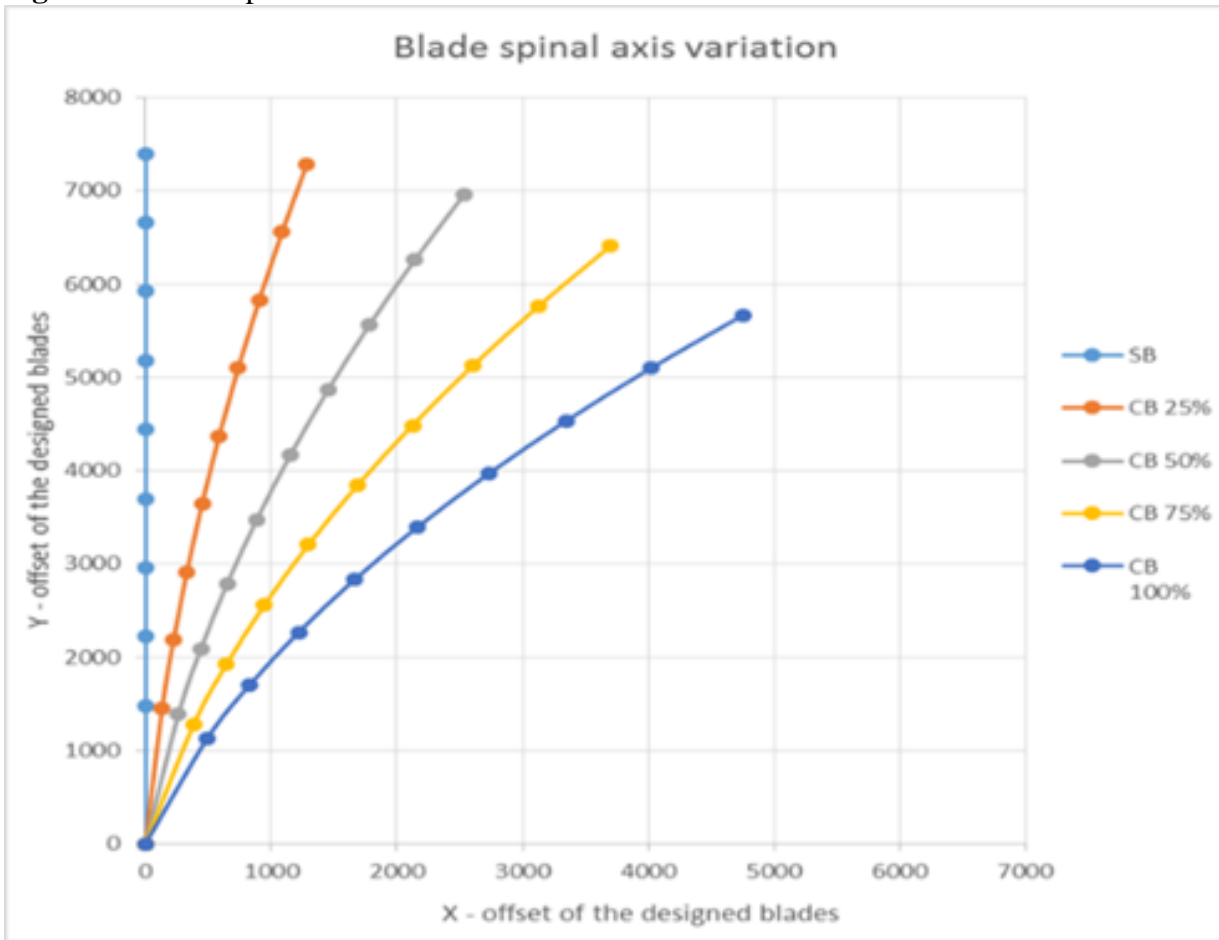
669
670

671 **Figure 7** - Inlet, Outlet, and Height Extension from the Turbine Blades
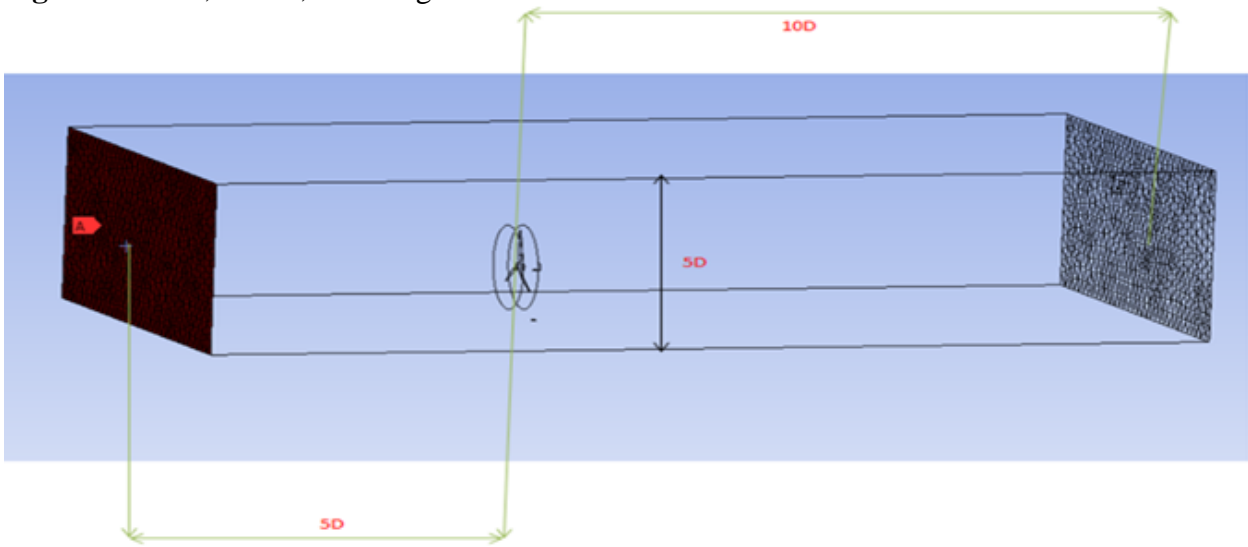
672
673
674
675

676

Table 3 Mesh size, CFD simulation time, and estimated C_P for SST model at $\lambda = 5$.

Mesh Resolution	Coarse Mesh (M1)	Medium mesh (M2)	Fine mesh (M3)
Number of nodes	79859	151740	230439
CFD simulation time	4hrs 10mins	6hrs 16mins	9hrs 53mins
Estimated C_P	0.3816	0.4169	0.4218

677

678

679

680

681

682

683

684

685

686

687

688

689

690

691

692

693

694

695

696

697

698

699

700

Table 4 Mesh size, CFD simulation time, and estimated C_P for k-ε model at λ = 5.

Mesh Resolution	Coarse mesh (M4)	Medium mesh (M5)	Fine mesh (M6)
Number of nodes	44064	92767	139506
CFD simulation time	1hr 36mins	4hrs 41mins	5hrs 38mins
Estimated C_P	0.2271	0.2586	0.2693

701
702
703
704
705
706
707
708
709
710
711
712
713
714
715
716
717
718
719
720
721
722
723
724
725
726
727
728
729
730
731
732
733
734
735
736
737

738   *Figure 8 The power coefficients of all the investigated meshes in mesh independency study*

739
740
741
742
743
744
745
746
747
748
749
750
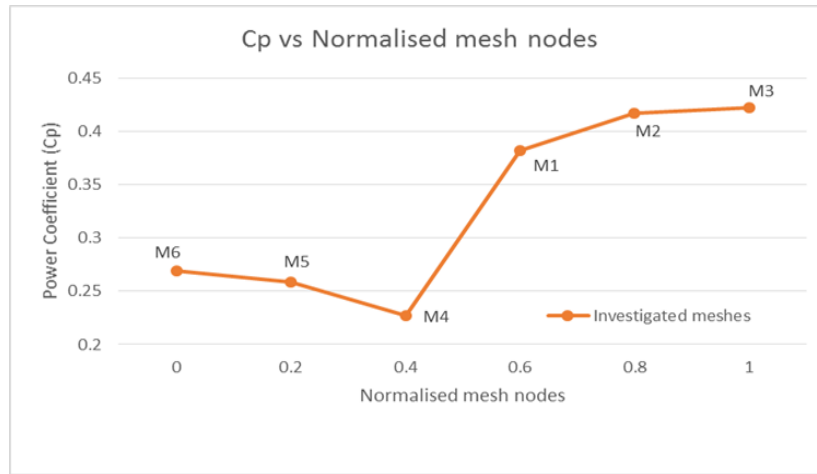
787
788
789
790 *Figure 9 Torque coefficient versus Tip speed ratio for k-ε and SST model medium meshes*
791
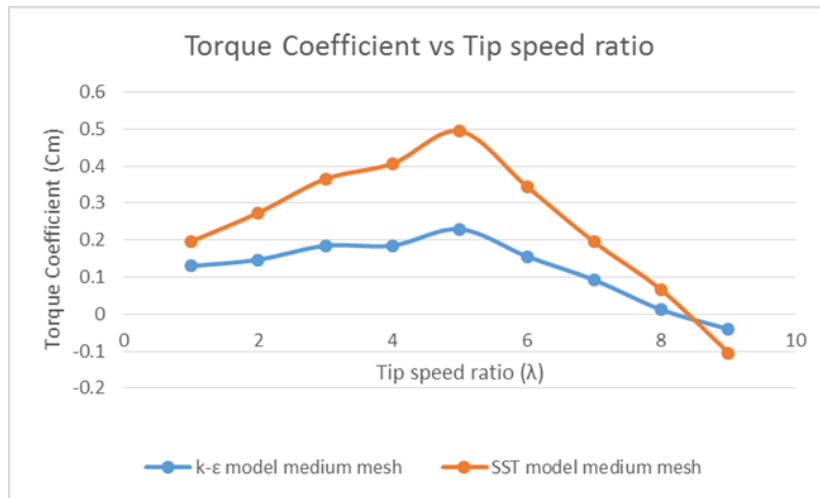
792
793
794
795
796
797
798
799
800
801
802
803
804
805
806
807
808
809
810
811
812
813
814
815
816
817
818
819
820
821
822

825 *Figure 10 Power coefficient versus tip speed ratio for k-ε and SST model medium meshes*

Cp vs Tip speed ratio
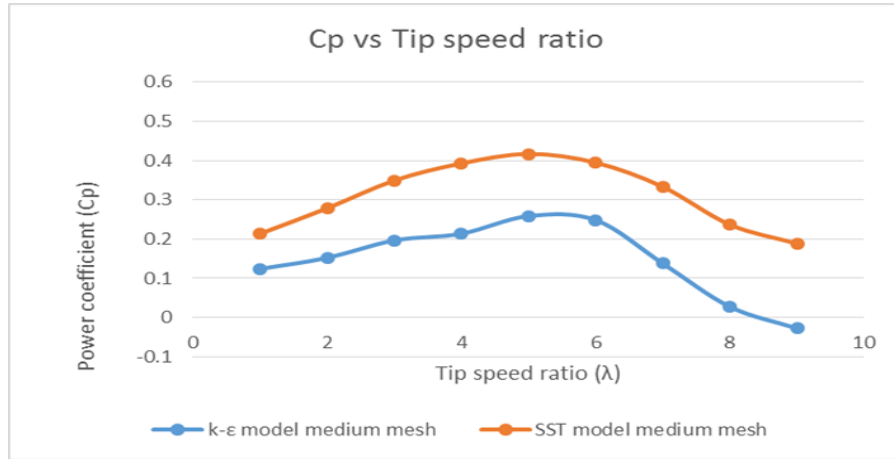
873
874
Figure 11 - a) Meshed SB with Blades and Hub, b) SB Meshed Tip, c) Meshed 75% CB with Blades and Hub, d) 75% CB Meshed Tip
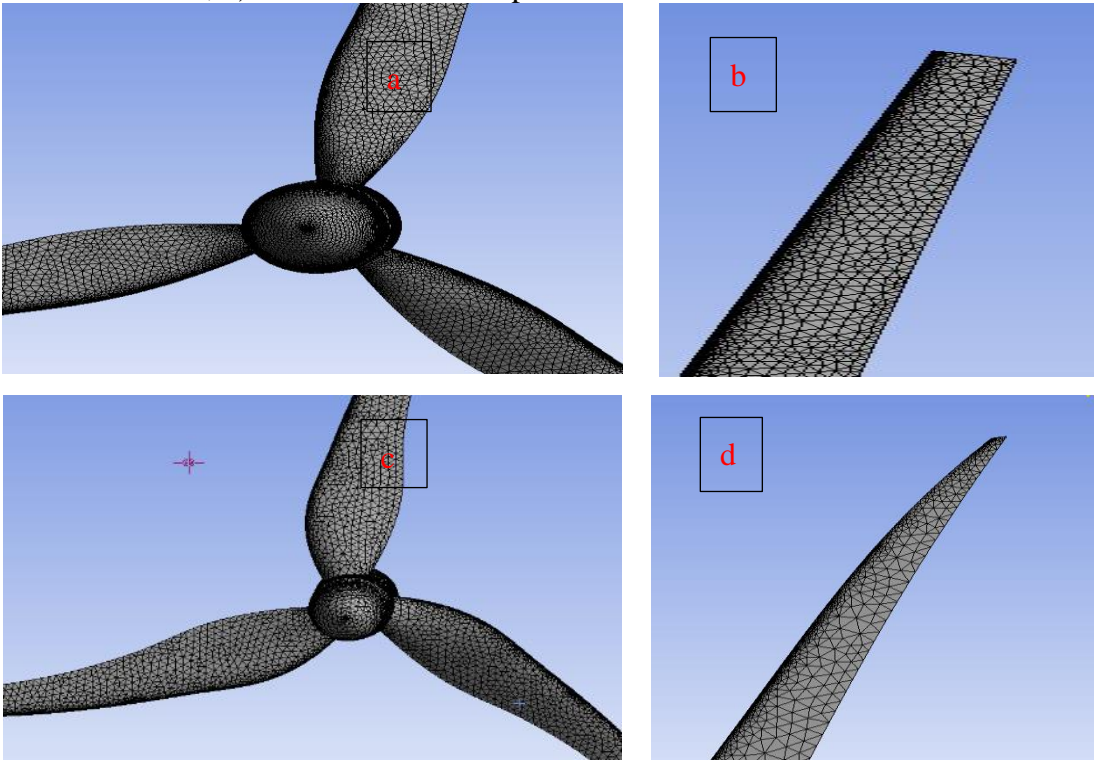

877
878

879 **Table 5** - Mesh Parameters for all the Designed Blades (SST)

Blade Model	Mesh growth rate	Maximum mesh size (mm)	Minimum mesh size (mm)	Curvature normal angle (°)	Number of nodes
SB	1.2	2500	75	15	151740
CB 25%	1.15	2100	50	13	195647
CB 50%	1.10	1800	45	11	226846
CB 75%	1.05	1500	40	10	252839
CB 100%	1.0	1150	35	10	309461

880
881
882

Figure 12 - Blade Pressure Distributions (Pressure Side) on a) SB, b) CB 25 %, c) CB 50%, d) CB 75%, and e) CB 100%
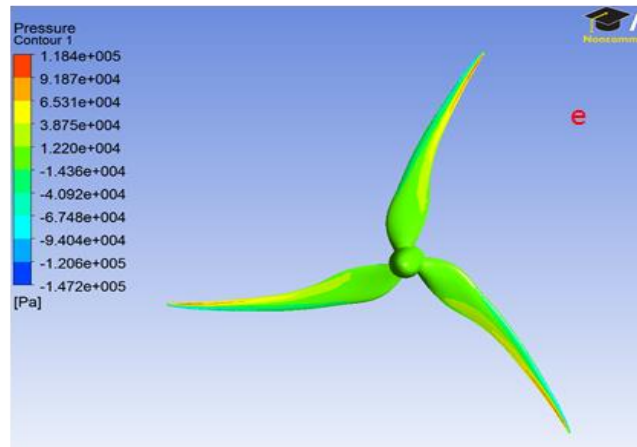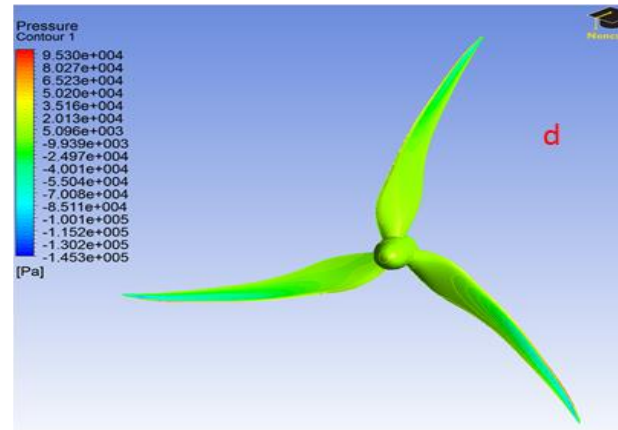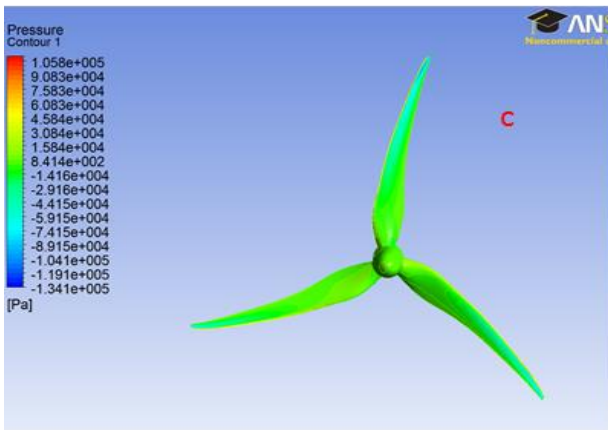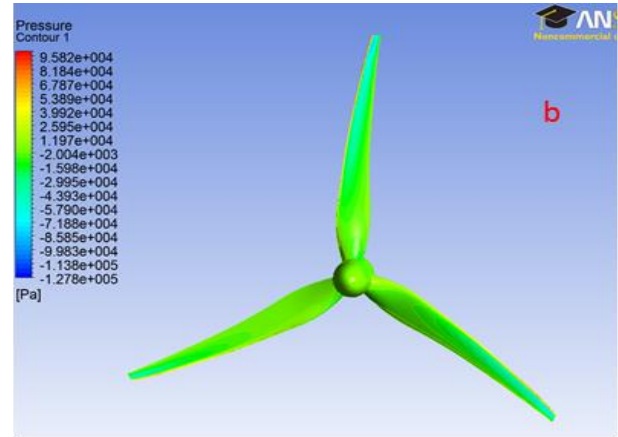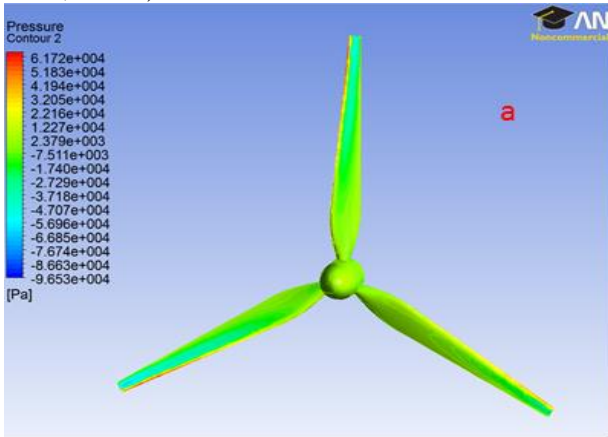
888 **Figure 13** - SST Mid-height Lift Coefficient Distribution for Five Blade Designs
889
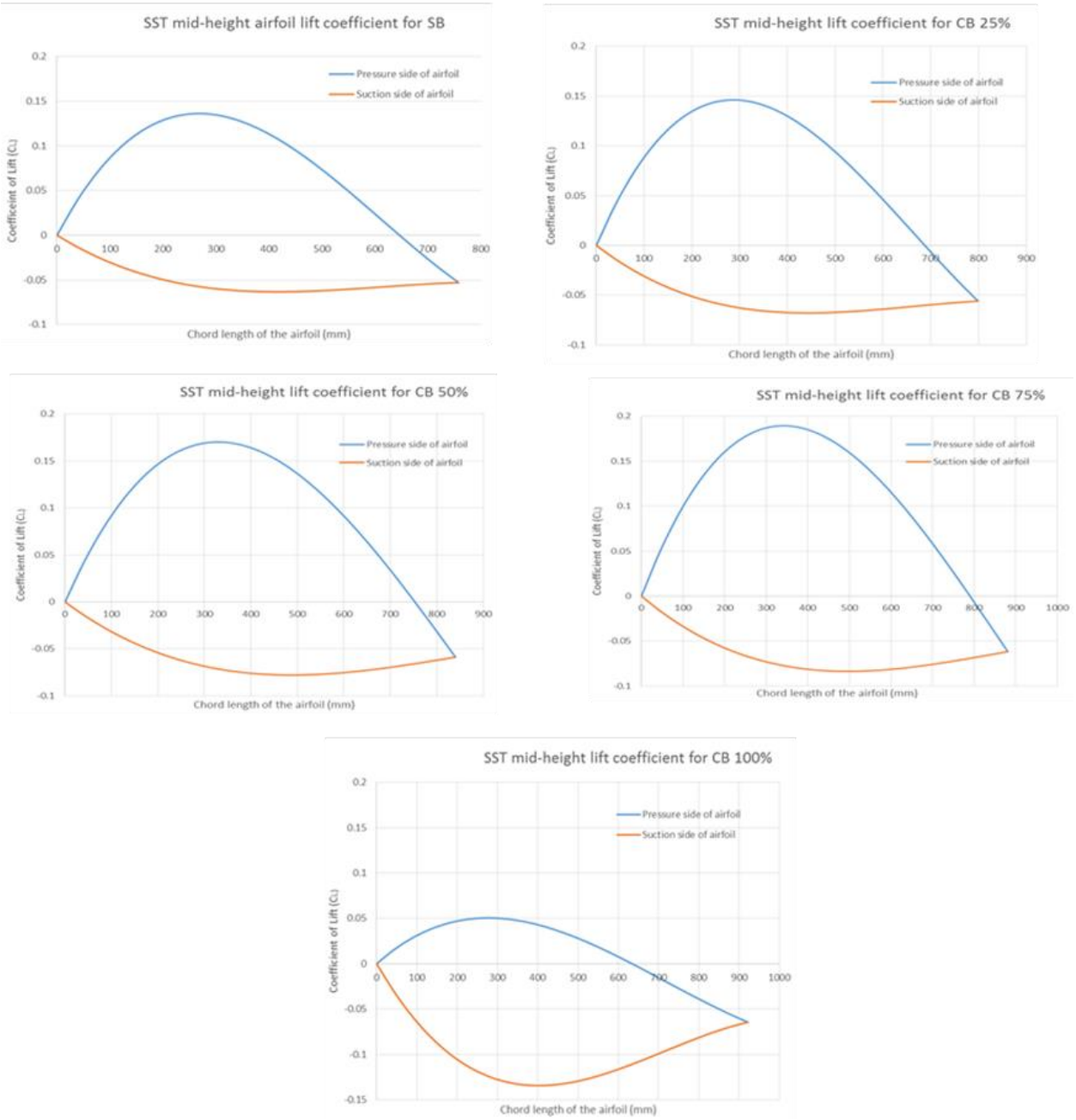
890
891
892

893   **Table 6** - Mesh Parameters for the Designed Blades (LES-Smagorinsky)

Blade Model	Mesh growth rate	Maximum mesh size (mm)	Minimum mesh size (mm)	Curvature normal angle (°)	Number of nodes
SB	1.0	1150	65	10	427552
CB 25%	0.85	950	45	9	514842
CB 50%	0.7	820	40	7	690137
CB 75%	0.55	760	38	6	851326
CB 100%	0.4	680	35	6	912470

894
895

896　**Figure 14** - CB 75% LES-Smagorinsky Convergence Monitoring with Respect to the Defined
897　Convergence Criteria.
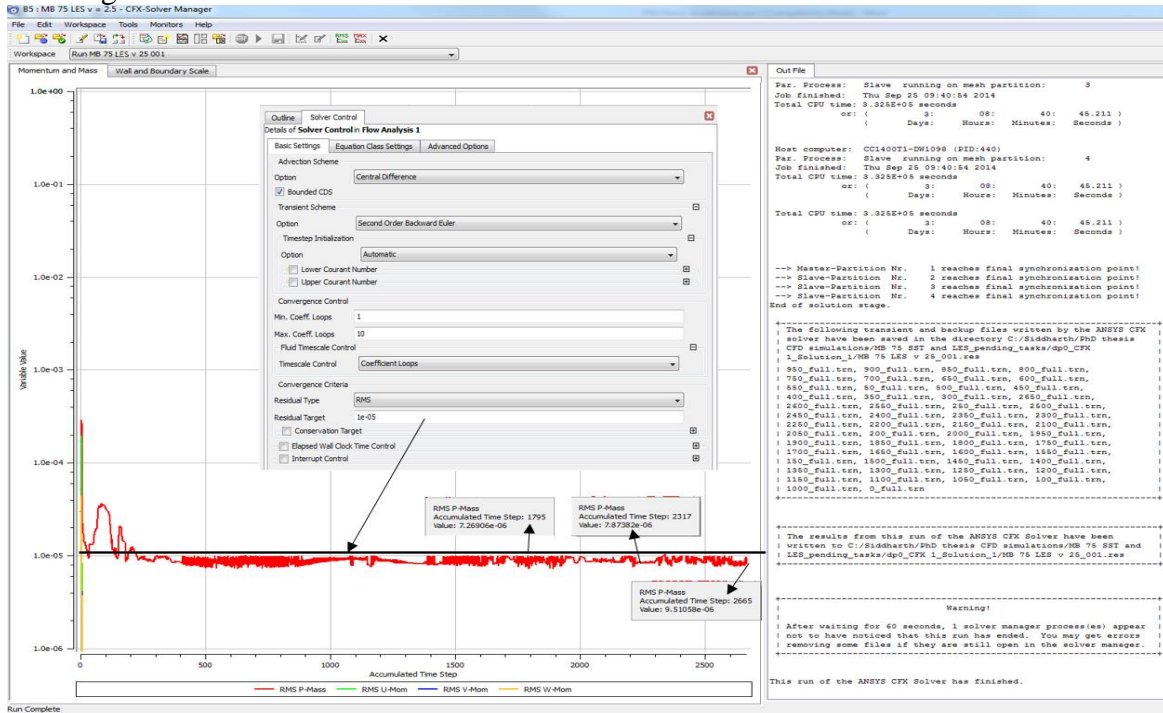
898
899
900

901 **Figure 15** - Lift Coefficient History Convergence Monitoring for the CB 75% Transient Solution.
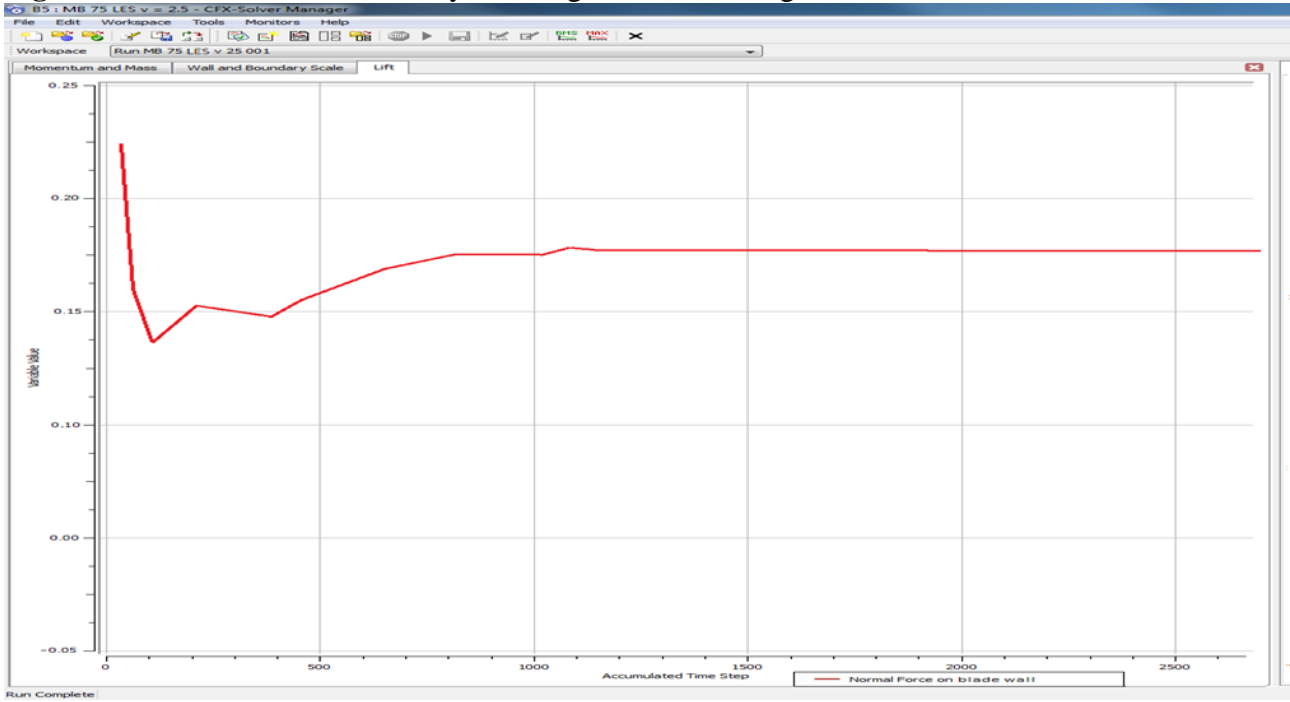

902
903
904
905
906

907 **Figure 16** – LES-Smagorinsky Blade Pressure Distributions (Pressure Side) on a) SB, b) CB 25 %,
908 c) CB 50%, d) CB 75%, and e) CB 100%
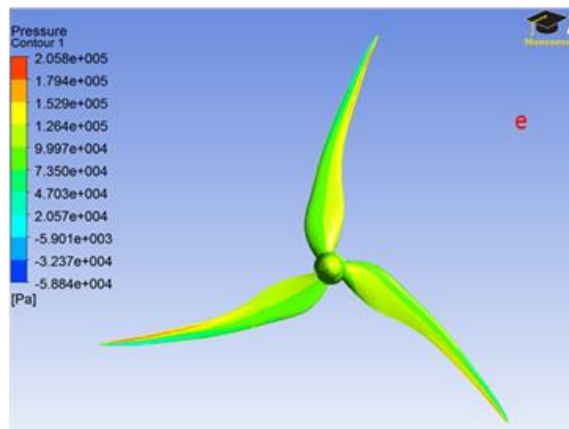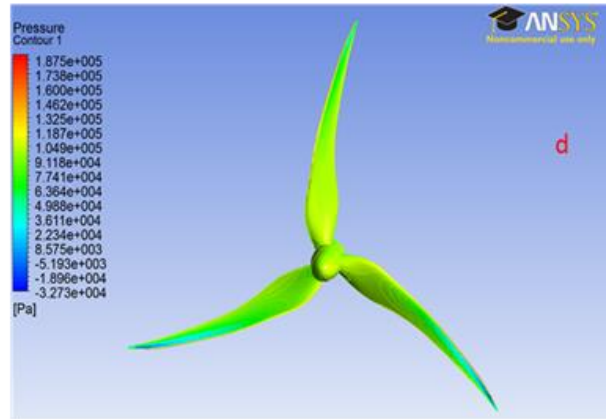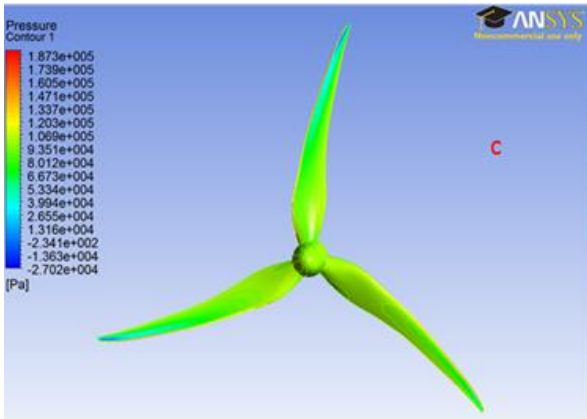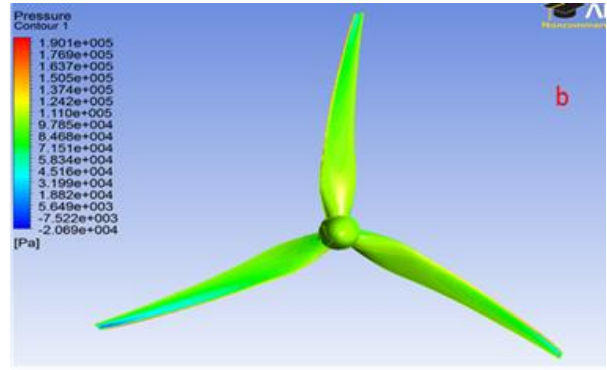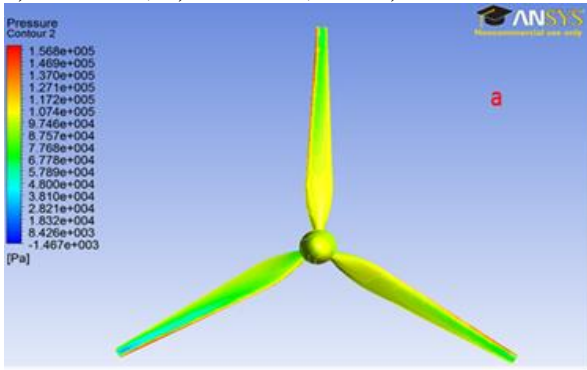
909
910
911

912 **Figure 17** - LES – Smagorinsky Mid-height Lift Coefficient Distribution for Five Blade Designs
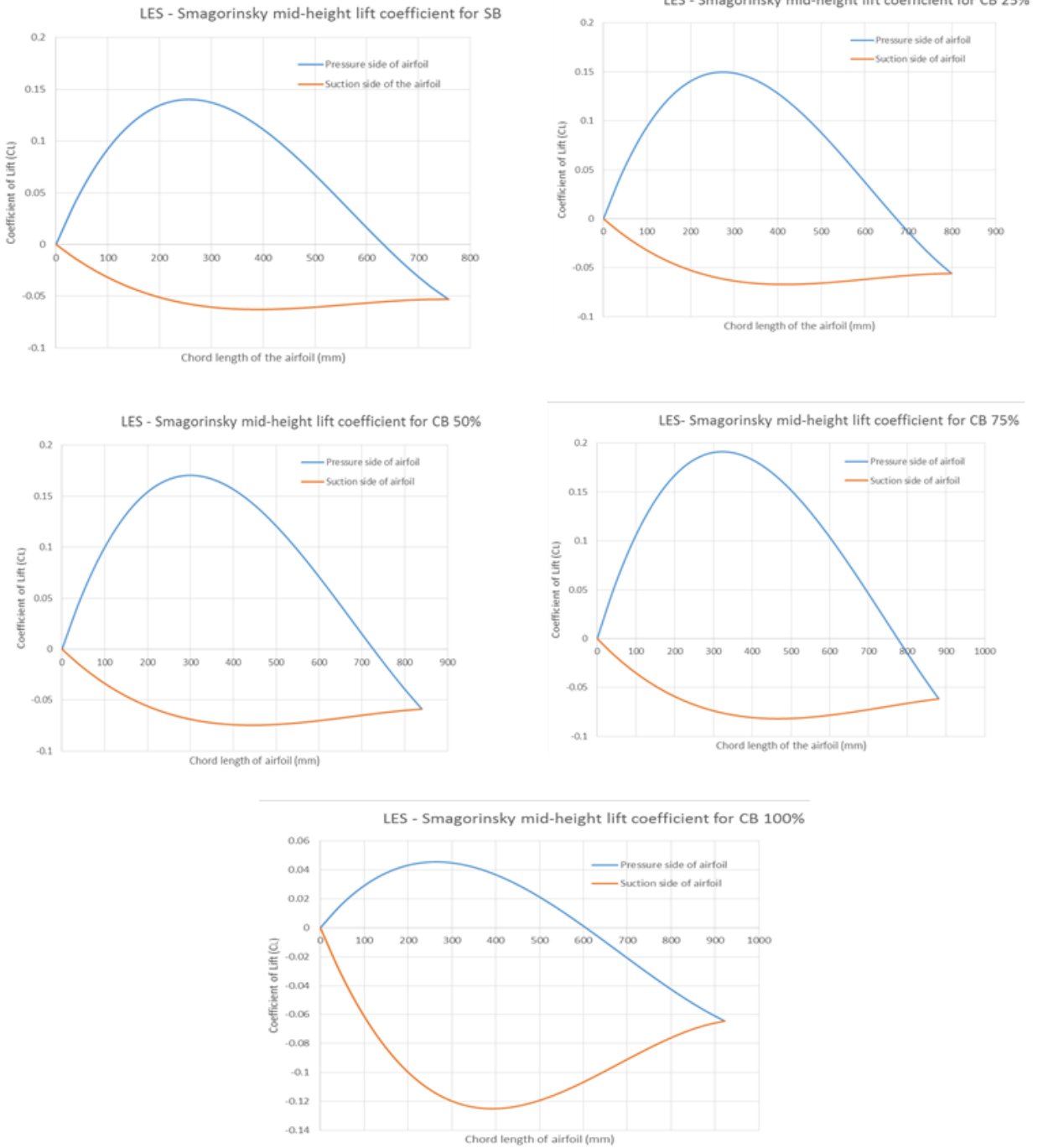

913
914
915

916 **Figure 18** - Lift Coefficient Versus Angle of Attack for SST and LES CFD Simulations, at Inlet
917 Velocity 2.5m/s
918
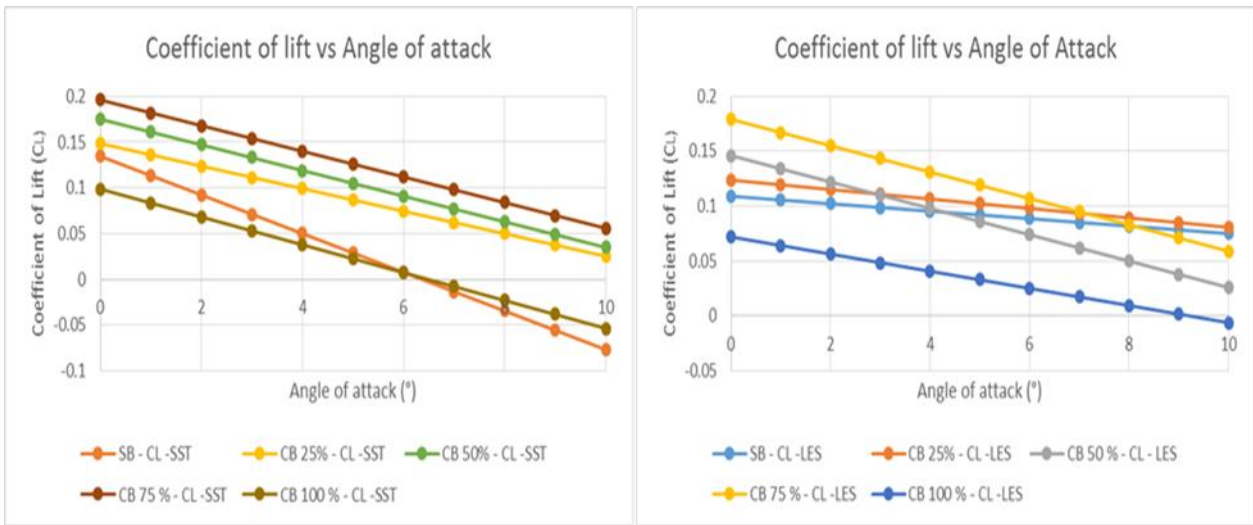
919
920

921 **Figure 19** - Power Coefficient Versus Output Power for the Designed Five Blades

922